RESEARCH ARTICLE | MARCH 05 2021

Blowing-only opposition control: Characteristics of turbulent drag reduction and implementation by deep learning

Zexiang Li (李泽祥) ; Xiangxin Dang (党向新) ; Pengyu Lv (吕鹏宇); Huiling Duan (段慧玲)

AIP Advances 11, 035016 (2021)
https://doi.org/10.1063/5.0042740

Blowing-only opposition control: Characteristics of turbulent drag reduction and implementation by deep learning

Cite as: AIP Advances 11, 035016 (2021); doi: 10.1063/5.0042740
Submitted: 16 February 2021 • Accepted: 23 February 2021 •
Published Online: 5 March 2021

Zexiang Li (李泽祥),[1,2] Xiangxin Dang (党向新),[1] Pengyu Lv (吕鹏宇),[1] and Huiling Duan (段慧玲)[1,2,a)]

AFFILIATIONS

[1] State Key Laboratory for Turbulence and Complex Systems, Department of Mechanics and Engineering Science, BIC-ESAT, College of Engineering, Peking University, Beijing 100871, China

[2] Key Laboratory of High Energy Density Physics Simulation, Center for Applied Physics and Technology, Peking University, Beijing 100871, China

[a)] Author to whom correspondence should be addressed: hlduan@pku.edu.cn

ABSTRACT

Opposition control is an effective active control strategy for drag reduction, which has been extensively investigated. In the current work, the essential characteristics of drag reduction by the blowing-only opposition control scheme (i.e., opposition blowing) in turbulent channel flow are investigated. It is demonstrated that, under the condition of constant wall-normal mass flux, the drag reduction achieved by the opposition blowing scheme is almost independent of the allocation of the blowing velocity among all the effective blowing points. This feature simplifies the complexity of the control scheme and provides great convenience for the application of the convolutional neural network (CNN) to implement the opposition blowing scheme, i.e., only the direction of the wall-normal velocity at the detection plane needs to be predicted. In this paper, both the streamwise and spanwise wall shear stresses are taken as the input of the CNN model, and the reasonability of the CNN model is verified from a statistical perspective. It is found that as long as the directions of the large wall-normal velocity fluctuations are accurately predicted, the opposition blowing scheme can be successfully implemented, in which the CNN model is able to ensure a high prediction accuracy. Furthermore, applying the trained network model to a flow at a higher Reynolds number than the training set can still accurately predict the directions of the large wall-normal velocity fluctuations, which generalizes the applicability of the CNN model.

I. INTRODUCTION

Turbulent drag reduction is of great significance to reduce energy consumption and improve the performance of aircraft or underwater vehicles. The bursting processes induced by the near-wall streamwise vortices are responsible for the high skin-friction drag in wall turbulence, especially the sweep events.[1–3] Effective modulation or elimination of streamwise vortices by active or passive flow control schemes, such as spanwise oscillation,[4–9] opposition control,[10–18] and superhydrophobic surfaces,[19–27] can substantially reduce the skin-friction drag. As a concise feedback control strategy, opposition control, which was proposed by Choi *et al.*,[10] opens up an effective approach for turbulent drag reduction. By sensing the wall-normal velocity at the detection plane above the wall, the opposition control can effectively reduce the skin-friction drag through opposing the motion of near-wall turbulent structures by blowing and suction at the wall.

Different blowing or suction responses at the wall according to the detected wall-normal velocity lead to a variety of opposition control schemes, which have been widely investigated. The blowing response can reduce the skin-friction drag but enhance the turbulent fluctuations, while the suction response exhibits the opposite trend in both aspects. The original opposition control scheme conducted by Choi *et al.*[10] was to apply blowing and suction at the wall exactly opposite to the wall-normal velocity at the detection plane. A drag reduction of 25% can be achieved at the optimal detection

plane $y_d^+ \approx 10$, in which the control efficiency is optimistic.[10] y_d^+ is the non-dimensional distance from the detection plane to the wall scaled by the viscous length scale. When the detection plane deviates from the optimal position, the effect of opposition control on drag reduction deteriorates. According to Chung and Talha[13] and Deng *et al.*,[14] a substantial drag reduction can be achieved in a wide range above the wall by changing the amplitude of blowing and suction, and the drag reduction is positively correlated with the amplitude when the detection plane is located below 20 wall units. If the time delay between the sensor for the velocity at the detection plane and the actuator for the blowing and suction is considered, the sensor can be arranged within a certain distance upstream of the actuator, and the optimal detection plane locates at $y_d^+ \approx 20$.[16] Given the fact that the suction part of the opposition control is not conducive to the drag reduction,[10,28] Pamiès *et al.*[12] proposed the blowing-only opposition control scheme, which can significantly improve the drag reduction. However, in the scheme of blowing-only opposition control, the wall-normal mass flux is no longer zero. Therefore, it is necessary to compare the drag reduction of this scheme with that of the uniform blowing[28–34] at the same mass flux.

A key issue in the practical implementation of opposition control is that it is difficult to place sensors above the wall to obtain the required velocity information at the detection plane. Fortunately, many studies on turbulence physics have validated that the instantaneous wall shear stress is closely correlated with the coherent structures near the wall,[35–38] and it is feasible to obtain the force information at the wall. Therefore, it is the most promising way to predict the velocity distribution at the detection plane through the information at the wall, especially shear stresses and pressure.[39–44]

The neural network[45] provides a powerful tool for finding the correlation between physical quantities that cannot be analyzed mathematically, and the growing prosperity of deep learning algorithms[46–51] brings broader possibilities for fluid dynamics,[52–54] especially CNN. CNN provides a reduced-order description for flow field,[54–56] and its capability in flow field estimation[48,49,57,58] and reconstruction[50,58] has been widely proved. According to Güemes *et al.*,[57] the CNN models have the capability of tackling nonlinear features of wall-bounded turbulent flows. Sekar *et al.*[49] combined deep CNN with a deep multilayer perceptron to predict the incompressible laminar flow over airfoils. The results indicate that the approach is efficient and accurate. Peng *et al.*[48] proposed an unsteady data-driven reduced-order model to predict the velocity field around an airfoil. In their work, a CNN model is applied as the encoder to extract the spatial and temporal features of the flow field, and a deconvolutional neural network (DCNN) works as the decoder to reconstruct the information. The feasibility of the CNN–DCNN model is proved. Wang *et al.*[58] developed a CNN model to improve the spatial resolution of the turbulent velocity fields obtained by particle image velocimetry. It is demonstrated that the CNN model can predict the missing information and enhance the spatial resolution of the near-wall velocity fields.

In terms of turbulence control for drag reduction, Lee *et al.*[39] first applied a neural network to carry out the opposition control scheme. Depending on the wall shear stress in the spanwise direction, the wall-normal velocity at $y_d^+ = 10$ was predicted, and the strategy of blowing and suction on the wall based on the neural network can achieve a drag reduction of 20%. Lorang *et al.*[43] also performed a neural network to predict the wall-normal velocity at $y_d^+ = 10$ through the spanwise wall shear stress. The primary difference between Lee *et al.*[39] and Lorang *et al.*[43] is that the former estimates the velocity value in the physical space while the latter manipulates the wavelength in the spectral space. Recently, Han and Huang[59] designed and trained different CNN models for the streamwise or the spanwise wall shear stress to predict the wall-normal velocity at the detection plane. They also verified that the CNN models could achieve substantial drag reduction in turbulent channel flow at different Reynolds numbers. In the above works, only the streamwise or the spanwise wall shear stress is used as the input of the neural network models to perform the prediction.

In the current work, in order to have a comprehensive understanding of the drag reduction characteristics of the blowing-only opposition control scheme (i.e., opposition blowing) in turbulent channel flow, the effect of the allocation of the blowing velocity on drag reduction under a constant blowing mass flux is investigated. The allocation of the blowing velocity refers to the velocity or mass flux allocated to each effective blowing point according to the control scheme. From the view of the drag reduction properties, the drag reduction is demonstrated to be almost independent of the allocation of the blowing velocity among all the effective blowing points. Only the direction of the wall-normal velocity at the detection plane needs to be detected or predicted. The constructed CNN model can accurately predict the directions of the large wall-normal velocity fluctuations, which ensures the successful implementation of the opposition blowing scheme. Furthermore, the trained CNN model is examined to be generalized to the case of a higher Reynolds number than the training set.

This paper is organized as follows. In Sec. II, the opposition blowing scheme is presented as well as the effect on drag reduction. The mechanism of drag reduction is also analyzed. In Sec. III, the correlation between the wall shear stresses and the wall-normal velocity at the detection plane is confirmed from a statistical perspective so as to clarify the rationality of the CNN model. In Sec. IV, the CNN model is constructed to carry out the opposition blowing scheme. The training process of the CNN model is discussed in Sec. IV A, *a priori* and *a posteriori* tests are conducted in Sec. IV B, and the CNN model is generalized to a higher Reynolds number in Sec. IV C. Finally, in Sec. V, the conclusions are presented.

II. OPPOSITION BLOWING SCHEME

The control scheme is implemented in a fully developed turbulent channel flow (Fig. 1) at $\mathrm{Re}_{\tau 0} = 180$ by direct numerical simulation (DNS), where $\mathrm{Re}_{\tau 0}$ is the friction Reynolds number based on the friction velocity $u_{\tau 0}$ and the half channel height h. The Fourier–Chebyshev pseudospectral method is employed to solve

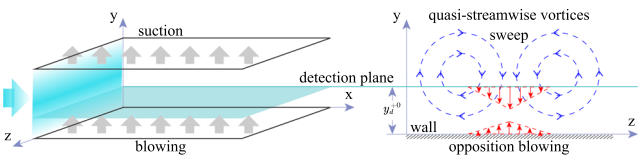

FIG. 1. Schematic of the opposition blowing scheme.

the Navier–Stokes equations. The DNS program used in the current work can distinguish the highest wavenumber, so that any discontinuous boundary conditions given in the physical space can be accurately identified (see details in Appendix B). The domain size is $L_x = 4\pi h$, $L_y = 2h$, and $L_z = 2\pi h$, and the grid size is $N_x = 128$, $N_y = 128$, and $N_z = 128$ in the streamwise (x), wall-normal (y), and spanwise (z) directions, respectively.[60] Periodic boundary conditions are used in the streamwise and spanwise directions. The mean streamwise pressure gradient is adjusted in each time step to maintain a constant flow rate. The opposition blowing scheme at the lower wall of the channel is designed as

$$v\left(x,0,z,t^{n+1}\right) = \begin{cases} A(t)\left|v\left(x,y_d^{+0},z,t^n\right)\right|^{\alpha}, & v\left(x,y_d^{+0},z,t^n\right) < 0, \\ 0, & v\left(x,y_d^{+0},z,t^n\right) \geq 0, \end{cases} \quad (1)$$

where $v\left(x,y_d^{+0},z,t^n\right)$ is the wall-normal velocity at the detection plane in the current time step and $v\left(x,0,z,t^{n+1}\right)$ is the blowing velocity at the lower wall in the next time step. The detected wall-normal velocity of the current time step is used to decide the boundary condition of the next time step. Hereafter, the superscript +0 denotes the normalization by the viscous scales of the turbulent baseline flow. Note that the turbulent baseline flow refers to the fully developed uncontrolled flow and the flow in which the blowing scheme is applied is called the controlled flow. The coefficient $A(t)$ is adjusted in each time step to maintain a constant blowing mass flux BF, i.e., the averaged wall-normal mass flux, and

$$BF = \frac{1}{N_x N_z} \sum_{i,k=1,1}^{N_x,N_z} \rho v(i, j = 0, k, t), \quad (2)$$

where i, j, and k are the x, y, and z grid indices, respectively, ρ is the fluid density, and $v(i, j = 0, k, t)$ is the blowing velocity at the lower wall. In the current work, unless otherwise noted, the blowing mass flux is always constrained as a constant to ensure that the wall-averaged blowing velocity is 0.5% of the bulk mean velocity U_b, i.e., $BF = 0.005\rho U_b$. The wall-normal velocity at the upper wall in each time step is completely consistent with that of the lower wall (i.e., blowing at the lower wall and suction at the upper wall) to maintain a constant wall-normal mass flux. Similar settings of the boundary condition in turbulent channel flow have been reported in the literature to investigate the uniform blowing.[29,32] The schematic of the opposition blowing scheme is illustrated in Fig. 1.

In this control scheme, the distribution of effective blowing points at the wall is determined by and identical to the location distribution of the velocities toward the wall at the detection plane, while the allocation of the blowing velocity at each instant is regulated by α in Eq. (1). This indicates that the opposition blowing scheme in the current work is a kind of blowing scheme with real-time feedback from the detection plane, i.e., under the guidance from the detection plane. When $\alpha = 1$, the blowing velocity at each effective blowing point is proportional to the detected wall-normal velocity at the corresponding point of the detection plane right above the blowing point. When $\alpha = 0$, the velocities at all the effective blowing points are the same. Figure 2 illustrates the different allocations of the blowing velocity regulated by different α. As α decreases, the fluctuation of the blowing velocity is smoothed, and the velocity difference among the effective blowing points decreases until the difference disappears when $\alpha = 0$.

The drag reduction DR is quantified as the relative change in the mean skin-friction coefficient of the lower wall,

$$DR = \frac{\langle C_{f,0}\rangle - \langle C_f\rangle}{\langle C_{f,0}\rangle}, \quad (3)$$

where $\langle C_{f,0}\rangle$ and $\langle C_f\rangle$ are the mean skin-friction coefficients of the turbulent baseline flow and the controlled flow, respectively. Note that $\langle\cdot\rangle$ denotes the ensemble average over the entire lower wall as well as over the time after the flow reaches the statistically steady state. As an active control scheme, the control gain on the blowing side is of great interest. The control gain G is defined as the ratio of the saved power due to drag reduction to the input power of blowing,

$$G = \frac{(\langle\tau_{w,0}\rangle - \langle\tau_w\rangle)U_b}{W_{in}}, \quad (4)$$

where $\langle\tau_{w,0}\rangle$ and $\langle\tau_w\rangle$ are the mean streamwise shear stress at the lower wall without and with opposition control, respectively. $W_{in} = \langle|0.5\rho v^3|\rangle$ is the mean input power. Similar to the work of Kametani *et al.*,[28,32] an ideal situation is discussed in the current work, i.e., only the kinetic energy input is considered. The power consumption from the pressure difference between both sides of the blowing plate is not included.

In the opposition blowing scheme, as the flow structure above the wall evolves over time, the distribution and the number of effective blowing points at the wall change accordingly, resulting in the variation in the area fraction of the blowing points over the wall. The area fraction AF is the ratio of the amount of the effective blowing points to the total points at the lower wall, whose effect on the drag reduction remains unclear. Thus, stochastic blowing is performed to examine the influence of AF on the drag reduction and the control

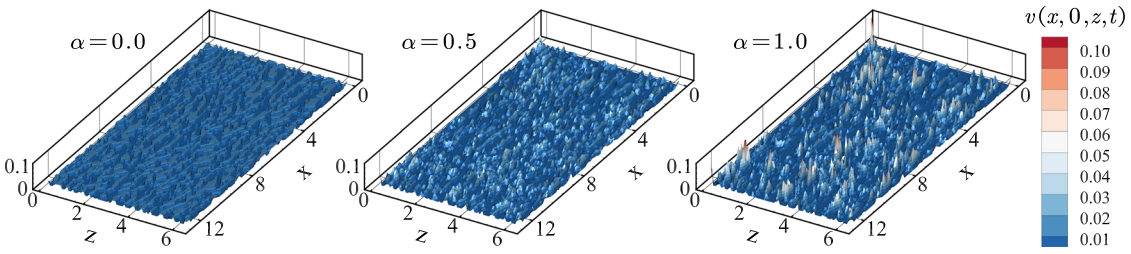

FIG. 2. The allocations of the blowing velocity at the lower wall at a certain instant for different α when the same detection plane information is detected.

gain. The stochastic blowing here refers to a control scheme that for a certain AF, an identical amount of blowing points are randomly selected in each time step, and the blowing velocity of each effective blowing point is the same. It should be noted that when $AF = 1$, the whole lower wall is blowing, i.e., the situation of uniform blowing. Compared to the control scheme Eq. (1), the stochastic blowing is independent of the guidance from the detection plane. DR and G achieved by the stochastic blowing scheme for different AF under $BF = 0.005\rho U_b$ are shown in Figs. 3(a) and 3(b), respectively. A remarkable feature is that the drag reduction is independent of AF, but the control gain is positively correlated with AF. Therefore, it is demonstrated that the effect of the area fraction on the drag reduction can be neglected.

DR and G of the opposition blowing scheme are shown in Figs. 4(a) and 4(b), respectively. Under a constant BF, the drag reduction increases monotonically as the distance from the detection plane to the wall decreases. In the height range of the detection plane investigated in the current work, the drag reduction of opposition blowing is higher than that of uniform blowing. For example, when $y_d^{+0} = 13.7$ and $\alpha = 0$, DR is ~0.46, which improves the drag reduction by around 17% compared to $DR \approx 0.39$ of uniform blowing. As the drag reduction achieved by a blowing scheme without guidance (i.e., stochastic blowing or uniform blowing) is almost constant under a constant BF as shown in Fig. 3(a) (i.e., $DR \approx 0.39$ under $BF = 0.005\rho U_b$), it is demonstrated that a blowing scheme with guidance (e.g., opposition blowing in the current work) can be more effective in drag reduction than that without guidance. Furthermore, under a constant BF, the distribution of the blowing points is more important than the allocation of the blowing velocity for the enhancement of drag reduction. In terms of the control gain, the closer the distance from the detection plane to the wall, the lower the control gain. The drag reduction and the control gain have the opposite variation trends as a function of the detection plane height.

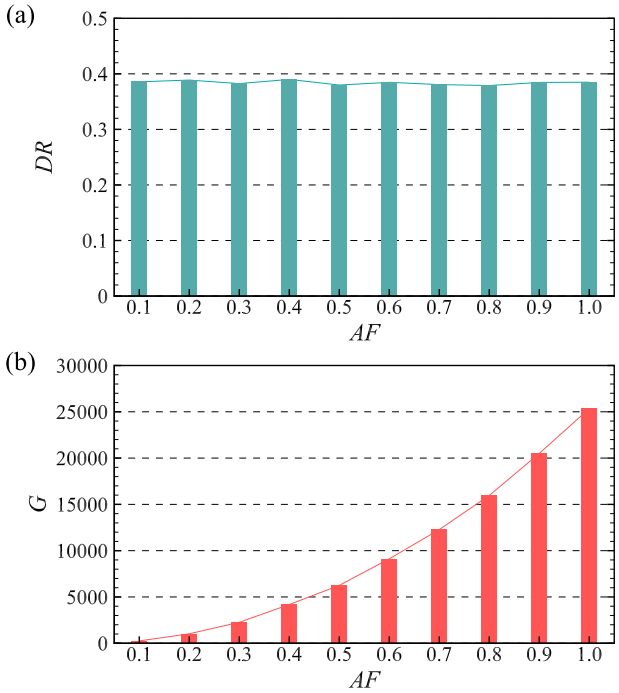

FIG. 3. (a) DR and (b) G of the stochastic blowing scheme for different AF under a constant BF.

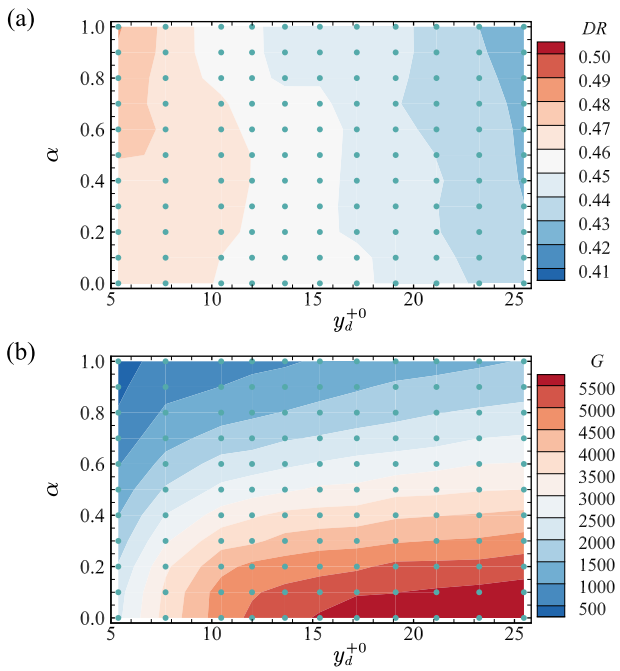

FIG. 4. (a) DR and (b) G of the opposition blowing scheme in the current work. The horizontal and vertical coordinates of the dots represent the parameters of the DNS cases. There are 121 cases in each figure.

For the completeness of the study, the drag increase on the suction side of the channel is investigated. Denote that the drag increase DI has the same expression as DR, i.e., Eq. (3). On the suction side, the skin-friction drag increases significantly. Although the positions of the suction points at the upper wall of the channel are the same as the blowing points at the lower wall at each instant, the temporal evolutions of the flows in the upper and lower parts of the channel are different. Therefore, the correlation between the suction velocity and the wall-normal velocity fluctuations in the near-wall region of the upper wall is not significant. Reflected in the skin-friction drag, DI of the 121 cases (Fig. 4) does not show regular changes like DR, but concentrates around a certain value, as shown in Fig. 5.

Besides, due to the asymmetric boundary conditions of the upper and lower walls (i.e., blowing at the lower wall and suction at the upper wall), the upper and lower parts of the turbulent channel flow are also asymmetric, and their interaction is inevitable. In order to show that the drag reduction characteristics obtained from the cases with asymmetric boundary conditions are relatively robust, cases in which the boundary conditions of blowing and suction are symmetric at the upper and lower walls are conducted, i.e., both blowing and suction are applied at local regions of both the upper and lower walls. It is demonstrated that the drag reduction of

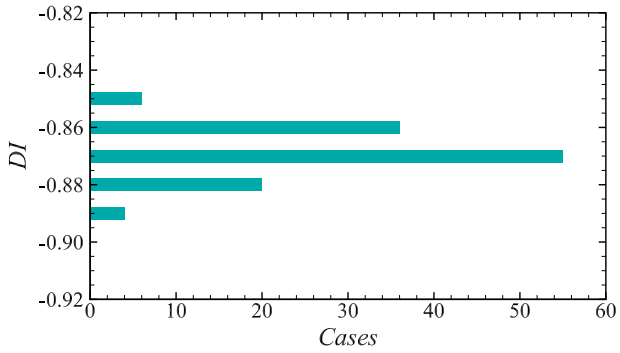

FIG. 5. *DI* at the upper wall of the channel. There are a total of 121 results, corresponding to the 121 cases in Fig. 4.

the opposition blowing scheme is still independent of the allocation of the blowing velocity among all the effective blowing points (see details in Appendix A).

As the allocation of the blowing velocity (i.e., α) has little effect on the drag reduction, the opposition blowing scheme, i.e., Eq. (1), can be simplified as

$$v\left(x,0,z,t^{n+1}\right)=\begin{cases}A(t), & v\left(x,y_d^{+0},z,t^n\right)<0,\\ 0, & v\left(x,y_d^{+0},z,t^n\right)\geq 0.\end{cases} \tag{5}$$

In the practical implementation, the opposition blowing scheme can be conducted as follows: selecting a detection plane, and then blowing uniformly (i.e., $\alpha = 0$) at all the points where the direction of the corresponding detected wall-normal velocity is toward the lower wall. In the circumstance of $\alpha = 0$, the complexity of the control scheme is distinctly reduced because the velocities of all the effective blowing points are the same. This brings great convenience to the application of CNN. Only the direction of the wall-normal velocity at the detection plane needs to be predicted. The construction of the CNN model in Sec. IV is based on this simplification.

The influence of opposition blowing on the flow in the near-wall region is addressed as follows, which also reveals the drag reduction mechanism. The vortices identified with the second invariant of the instantaneous velocity gradient tensor (i.e., the Q criterion[61]) are shown in Fig. 6. The background contour map of Fig. 6 is the wall-normal velocity fluctuations at $y^{+0} = 13.7$. As shown in Fig. 6, on the blowing side of the channel, the wall-normal velocity fluctuations in the near-wall region are enhanced, and the number of small-scale vortex structures also dramatically increases, which is related to the enhancement of local flow induced by the quasi-streamwise vortices. Figure 7 shows the wall-normal velocity fluctuations in a typical small region near the wall to illustrate this enhancement process of fluctuations. The location of this region has been marked by a small rectangle in Fig. 6. On the one hand, as the fluid on the downward moving side of the quasi-streamwise vortices is opposed by the opposition blowing, the impact of the sweep motion on the wall weakens, which will significantly reduce the skin-friction drag. On the other hand, the low-speed fluid introduced from the blowing region will move toward the adjacent non-blowing area under the induction of the quasi-streamwise vortices and continuously

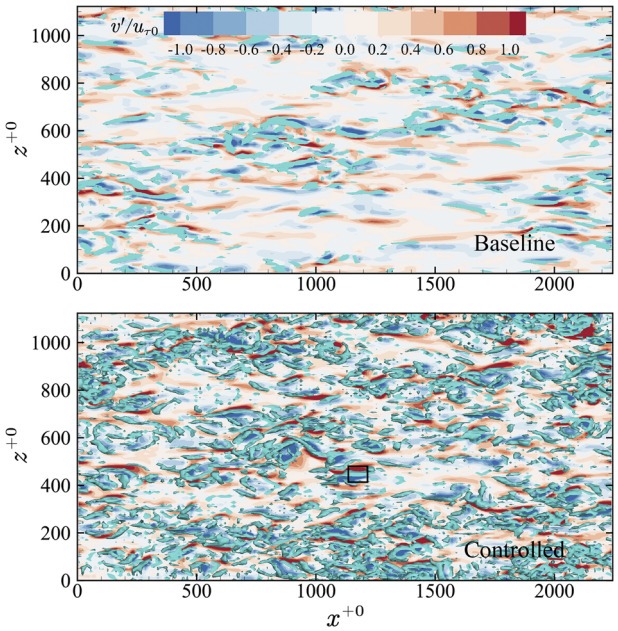

FIG. 6. Isosurfaces representing vortices below the wall-normal plane of $y^{+0} = 13.7$ identified by the Q criterion. $Q = 0.75$, normalized by the outer scale of the turbulent baseline flow, i.e., U_b^2/h^2. The background contour map is $v'/u_{\tau 0}$ at $y^{+0} = 13.7$, where v' is the wall-normal velocity fluctuation. The region marked by a small rectangle in this figure will be enlarged in Fig. 7. The controlled flow is under the control of opposition blowing with $\alpha = 0$ and $y_d^{+0} = 13.7$.

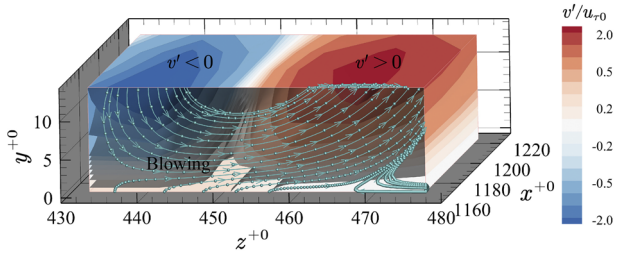

FIG. 7. Isosurfaces of the wall-normal velocity fluctuations in a small near-wall region. The lines in this figure are the streamlines located in the y–z plane with $x^{+0} = 1166$. The denseness of the points on the line represents the magnitude of the tangent velocity at that position. The denser the points, the smaller the velocity.

supply into the periphery of the vortices. As a result, the vortices in the near-wall region are strengthened.

III. VELOCITY–VORTICITY–VORTICITY CORRELATION

As mentioned above, the most promising way is to predict the velocity distribution at the detection plane through the measurable quantities at the wall, in particular, the wall shear stresses.[39,43,59] Thus, the principle of the CNN model in this paper is to predict the direction of the wall-normal velocity at the detection plane through the streamwise and spanwise wall shear stresses. As

long as the direction of the wall-normal velocity at the detection plane is obtained, the opposition blowing scheme can be realized naturally.

The correlation between the wall-normal velocity at the detection plane and the wall shear stresses is confirmed from a statistical perspective, i.e., the velocity–vorticity–vorticity correlation coefficient. The two-point cross correlation coefficient R_{ijk} between a velocity component (subscript i) at the reference point A and two vorticity components (subscripts j and k) at the variable point B is defined as

$$R_{ijk}(x_r, y_r, z_r; x, y, z) = \frac{\left\langle (u_i - \langle u_i \rangle)_A (\omega_j - \langle \omega_j \rangle)_B (\omega_k - \langle \omega_k \rangle)_B \right\rangle}{u_{i,rms}(y_r) \cdot \omega_{j,rms}(y) \cdot \omega_{k,rms}(y)}, \tag{6}$$

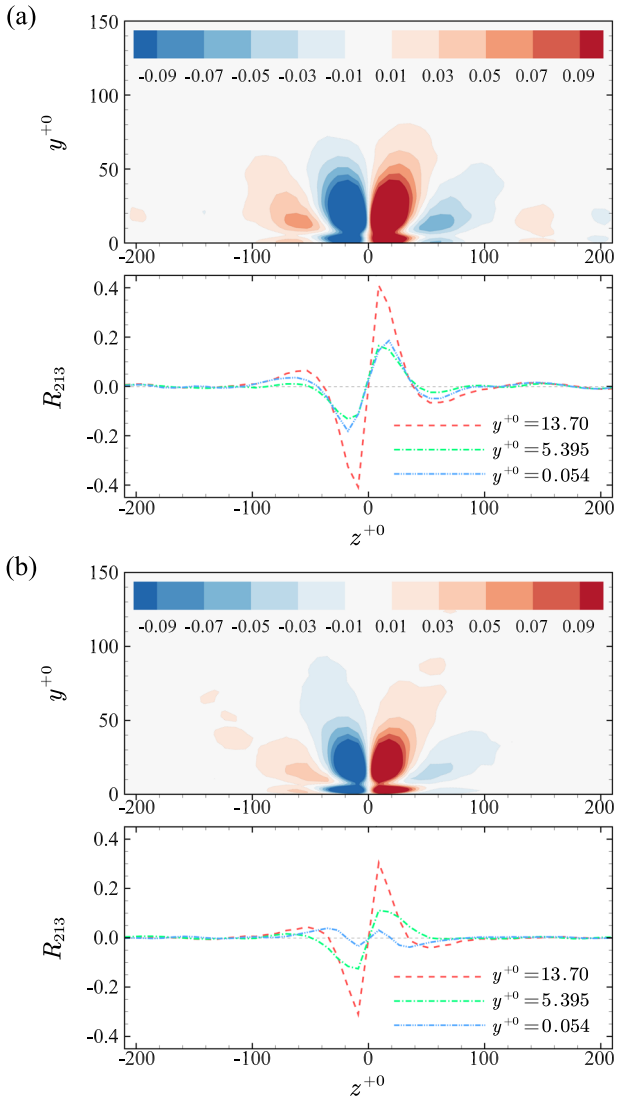

FIG. 8. The contours of R_{213} when $y_r^{+0} = 13.7$ in the section of $x^{+0} = 0$ as well as its variation along the spanwise direction at three wall-normal stations of (a) the turbulent baseline flow and (b) the controlled flow ($\alpha = 0$, $y_d^{+0} = 13.7$).

where (x_r, y_r, z_r) and (x, y, z) are the coordinates of the reference point A and the variable point B, respectively. After the ensemble average is performed in the horizontal direction, a corresponding spatial distribution of cross correlation coefficients $R_{ijk}(y_r; x, y, z)$ can be obtained for each reference height y_r. The value range of R_{ijk} is $[-1, 1]$.

The isosurfaces of R_{ijk} can be referred to as velocity–vorticity–vorticity correlation structure (*VVVCS*), which represents the topological relationship between the velocity at the reference height y_r and the surrounding vorticity field. Chen *et al.*[62] proposed the concept of velocity–vorticity correlation structure (*VVCS*) and described the structural characteristics of *VVCS* in detail. They have proved that the velocity component and the vorticity component in the flow field are closely correlated. In addition, *VVVCS* and *VVCS* have similar topological invariance. Therefore, the structural characteristics of *VVVCS* are not discussed in this paper.

According to the statistical properties of turbulent channel flow, the wall shear stresses and the vorticity satisfy the relationship of $\langle \partial w/\partial y \rangle = 2\langle \omega_x \rangle$ and $\langle \partial u/\partial y \rangle = -2\langle \omega_z \rangle$. Thus, the isosurface of R_{213} (i.e., $VVVCS_{213}$) characterizes the topology between the distribution of shear stresses in the channel and the wall-normal velocity at the reference plane. Figures 8(a) and 8(b) show the distributions of R_{213} ($y_r^{+0} = 13.7$) in the section of $x^{+0} = 0$ as well as the variation of R_{213} along the spanwise direction at three wall-normal stations of the turbulent baseline flow and the controlled flow ($\alpha = 0, y_d^{+0} = 13.7$), respectively. After the opposition blowing scheme is applied, the correlation in the near-wall region decreases obviously. A noteworthy feature is that the distribution of R_{213} along the spanwise direction presents a stable pattern, which is very similar to the coherent pattern of weight distribution obtained from the off-line training of neural networks conducted by Lee *et al.*[39] This characteristic manifests that: (i) there is a strong correlation between the wall-normal velocity at a specific wall-normal plane and the distribution of shear stresses in the channel, including the wall shear stresses; (ii) neural networks can capture the local characteristics of coherent structures. Hence, it is reasonable to construct a CNN model to link this correlation.

IV. CONVOLUTIONAL NEURAL NETWORK

According to the property that the drag reduction is independent of the allocation of the blowing velocity, the direction of the wall-normal velocity at the detection plane, i.e., $sgn(v)$, is considered as the ground truth for training and testing the network. The logical values of $sgn(v)$ include ±1 and 0, where −1 represents that the direction of the wall-normal velocity is toward the lower wall. The schematic of the constructed CNN model is illustrated in Fig. 9, and the architecture is listed in Table I.

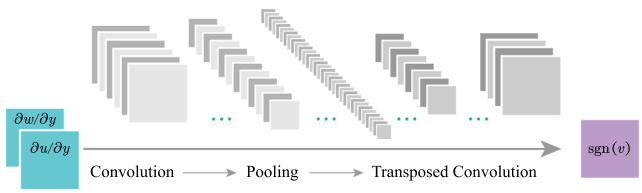

FIG. 9. Schematic of the CNN model.

TABLE I. The architecture of the CNN model. "conv2d" represents the two-dimensional convolution. "batchNorm" represents the batch normalization. "avePooling2d" represents the two-dimensional average pooling. "maxPooling2d" represents the two-dimensional maximum pooling. "transConv2d" represents the two-dimensional transposed convolution.

Num	Layer	Filter	Size
1	Image input	...	128 × 128 × 2
2	conv2d + batchNorm + leakyRelu	5 × 5	128 × 128 × 32
3	conv2d + batchNorm + leakyRelu	5 × 5	128 × 128 × 64
4	avePooling2d	...	64 × 64 × 64
5	conv2d + batchNorm + leakyRelu	5 × 5	64 × 64 × 128
6	conv2d + batchNorm + leakyRelu	5 × 5	64 × 64 × 256
7	maxPooling2d	...	32 × 32 × 256
8	conv2d + batchNorm + leakyRelu	3 × 3	32 × 32 × 128
9	conv2d + batchNorm + leakyRelu	3 × 3	32 × 32 × 64
10	transConv2d + leakyRelu	4 × 4	64 × 64 × 128
11	transConv2d + leakyRelu	4 × 4	128 × 128 × 64
12	conv2d + leakyRelu	3 × 3	128 × 128 × 32
13	conv2d	3 × 3	128 × 128 × 1
14	Regression output	...	128 × 128 × 1
15	Classification (*sgn*)	...	128 × 128 × 1

The two channels of the input layer contain the information of $\partial u/\partial y$ and $\partial w \partial y$ at the wall, respectively, while the output layer is the predicted $sgn(v)$ of the whole detection plane at the same time step. Two transposed convolution layers are used to extend the dimensions, which have been compressed by the average pooling and max pooling layers. Following the regression output layer, the classification layer is customized to divide all the positions into different categories, i.e., the predicted $sgn(v)$. In the current work, the CNN models were trained, tested, and implemented through the deep learning toolbox of MATLAB R2019b.

A. Model training

In terms of providing the dataset, 200 000 samples are generated from the evolution of the controlled turbulent channel flow ($\alpha = 0$, $y_d^{+0} = 13.7$). The non-dimensional time t^{+0} of the simulation ranges from 0 to 5800, and the time step is 0.029, normalized by $\nu/u_{\tau 0}^2$, where ν is the kinematic viscosity of the fluid. Each sample contains the distributions of $\partial u/\partial y$ and $\partial w/\partial y$ at the wall and the corresponding distribution of $sgn(v)$ at the detection plane. In the controlled flow, the implementation of the opposition blowing scheme starts from the 101st time step, so that the dataset contains the sample data from both the fully developed turbulent baseline flow and the controlled flow. The approach for selecting the training and validation sets is to select 50 000 samples in an orderly manner across the entire dataset, with a time interval of 0.116 between adjacent samples. Among these 50 000 samples, 40 000 samples are randomly selected as the training set, and the other 10 000 samples are defined as the validation set. The remaining 150 000 samples (i.e., the testing set) are used to examine the prediction accuracy of the CNN model.

All training and testing processes are implemented on a workstation equipped with a single NVIDIA GeForce RTX 2080Ti GPU with 11 GB VRAM. The training process of the CNN model has converged after 50 epochs, which takes around 7 h. Figure 10 shows the accuracy performance of the CNN model. Accuracy *acc* is defined as the ratio of the number of points that are correctly predicted to the total number of points at the detection plane, i.e., 128^2. The average accuracy of prediction on the validation set or the testing set is around 98.0% (legend "$\partial u/\partial y$ and $\partial w/\partial y$"). If the two channels of the input layer are replaced by a single channel containing only $\partial u/\partial y$ or $\partial w/\partial y$, while the architecture of the network remains unchanged, the prediction accuracy will decline. As shown in Fig. 10, the average accuracy on the whole dataset is 93.5% (legend "$\partial u/\partial y$ only") and 92.8% (legend "$\partial w/\partial y$ only") for the cases of $\partial u/\partial y$ and $\partial w/\partial y$, respectively. A very different feature from the previous literature[39,43] is presented here. For the CNN model in this paper, the network which takes the streamwise wall shear stress as the only input performs as well as that using the spanwise wall shear component. However, for the traditional neural network, the network performance based on $\partial w/\partial y$ is superior to that based on $\partial u/\partial y$.[39,43] This difference indicates that the traditional neural network cannot effectively correlate the streamwise wall shear stress to the wall-normal velocity at the detection plane, but the convolutional neural network here overcomes this limitation.

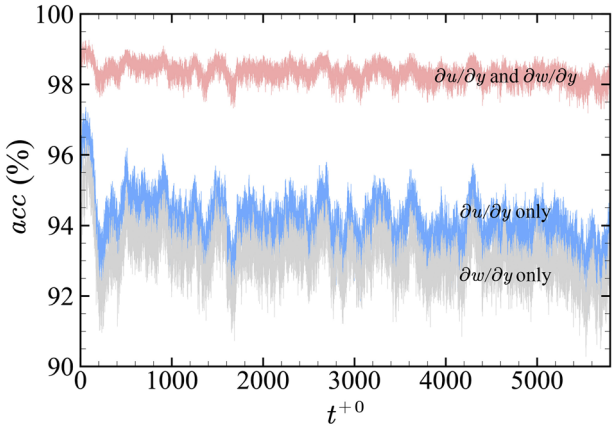

FIG. 10. Accuracy performance of the CNN model on the entire dataset.

In order to verify the robustness of the CNN model and evaluate the influence of the filter size, the prediction accuracy *acc*, the root-mean-square-error (*RMSE*), and the training time of the CNN model are compared when different filter sizes are selected in the first two convolutional layers, as shown in Table II. *RMSE* is defined as

$$RMSE = \sqrt{\frac{1}{n}\sum_{i=1}^{n}(X_t - X_r)^2}, \tag{7}$$

where n is the number of grid points at the detection plane of all validation samples, X_t is the ground truth at each grid point, and X_r is the regression output of the CNN model. The results show that increasing the filter size can only marginally improve the prediction accuracy and reduce the *RMSE*, whereas the training time of the model increases dramatically. Overall, the CNN model shows strong robustness.

TABLE II. Comparison of different filter sizes. "Filter-1" and "Filter-2" represent the filter sizes of the first and second convolutional layers. *RMSE* is the result of the regression layer when $sgn(v)$ is used as the ground truth. Time refers to the training time in minutes for 50 epochs.

Filter-1	Filter-2	*acc* (%)	*RMSE*	Time (min)
5 × 5	5 × 5	98.03	0.1269	430
7 × 7	5 × 5	98.06	0.1257	441
7 × 7	7 × 7	98.09	0.1249	572
9 × 9	5 × 5	98.13	0.1237	479
9 × 9	7 × 7	98.16	0.1228	578

B. *A priori* and *a posteriori* tests

To implement the opposition blowing scheme, the CNN model is combined with the DNS to take the place of velocity sensors at the detection plane. The predicted $sgn(v)$ of the detection plane is used to determine the distribution of blowing points at the lower wall. The routine implemented in the current work is to call the Matlab engine (which performs network prediction) from the main program (which calculates the flow field) and then returns the predicted $sgn(v)$ to the main program. Hence, the boundary condition of the next time step (i.e., the distribution of blowing points) is predicted by the wall shear stresses of the current time step.

The time histories of *acc* are shown in Fig. 11(a). The prediction accuracy declines rapidly over time, and *acc* eventually fluctuates around 64% (legend "network"). This accuracy performance is not up to expectations, and there is still room for improvement. A pertinent explanation is that the evolution of the flow field quickly develops to a different path from that of the training set after the opposition blowing is directed by the CNN model, resulting in the fact that the local characteristics are beyond the scope that the training set can recognize. Fortunately, the drag reduction can still be improved, as shown in Fig. 11(b) (legend "network"). Under $BF = 0.005\rho U_b$, *DR* obtained by the deep learning based opposition blowing scheme is ~0.42, which improves the drag reduction by about 8% compared to the value of uniform blowing.

In order to improve the network performance, the aforementioned training and validation sets are replaced by the new dataset, which is derived from the actual evolution of the flow field when the opposition blowing scheme is directed by the CNN model. Similarly, 50 000 samples with a time interval of 0.116 are saved for training and validation. Therefore, compared to the previous dataset, the turbulence state covered by the updated dataset is closer to the state when the network performs the prediction. For the network trained from the updated dataset, the network performance is obviously improved [legend "network-n," Fig. 11(a)]. Even the drag reduction of the deep learning based opposition blowing scheme [legend "network-n," Fig. 11(b)] exceeds the result of the $\alpha = 0$ scheme. Under $BF = 0.005\rho U_b$, *DR* obtained by the deep learning based opposition blowing scheme is ~19% higher than that of the uniform blowing.

Furthermore, another important factor affecting the prediction accuracy of the network is that the value of the wall-normal velocity at some points of the detection plane is very small, for instance, less than 0.1 times of the friction velocity $u_{\tau 0}$. In fact, the fluid at these points does not contribute to the major source of the skin-friction drag. Therefore, even though the predicted $sgn(v)$ values at these points are not correct, the influence on the drag reduction is not distinct. Figure 11(a) also shows the prediction accuracy without considering the wall-normal velocity in $[-0.1u_{\tau 0}, 0.1u_{\tau 0}]$ and $[-0.2u_{\tau 0}, 0.2u_{\tau 0}]$, which is about 85% (legend "network-n-1") and 90% (legend "network-n-2"), respectively. Figure 12 shows the comparison between the $sgn(v)$ predicted by the CNN model and the ground truth at a certain instant, which demonstrates that the CNN model can accurately predict the distribution of the large wall-normal velocity fluctuations at the detection plane. This feature gives strong evidence that the CNN model can provide practical guidance for opposition blowing.

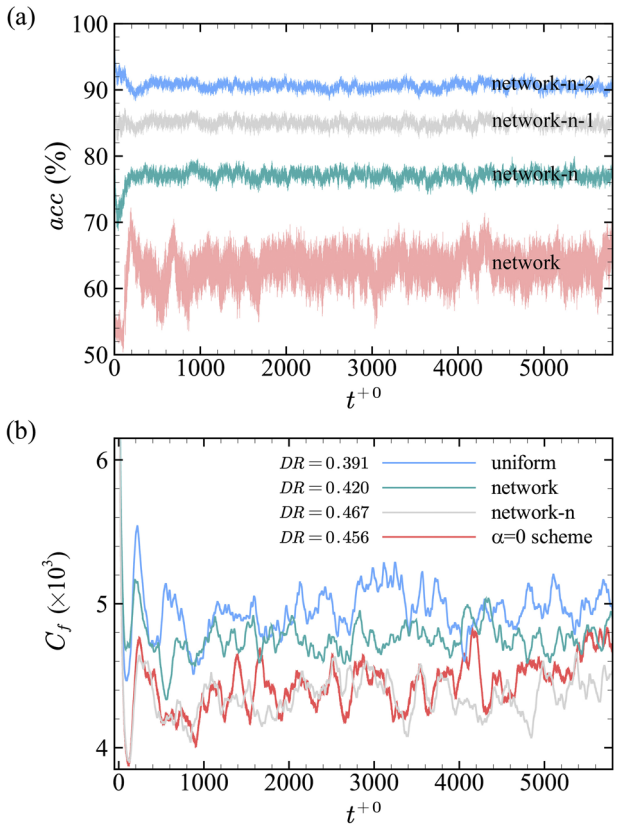

FIG. 11. (a) Time histories of *acc* after the velocity sensors at the detection plane are replaced by the CNN model. The implementation of the prediction starts from the 101st time step. (b) Comparison of the time histories of the wall-averaged skin-friction coefficient of the lower wall under different control schemes. "α = 0 scheme" represents the opposition blowing scheme in the current work without the CNN model.

C. Generalization to a higher Reynolds number

To generalize the study, the network trained from the case of $Re_{\tau 0} = 180$ is implemented to the case of $Re_{\tau 0} = 396$. The domain size for the case at a higher Reynolds number is $2\pi h \times 2h \times \pi h$, and the corresponding grid size is 256 × 256 × 256 in the streamwise,

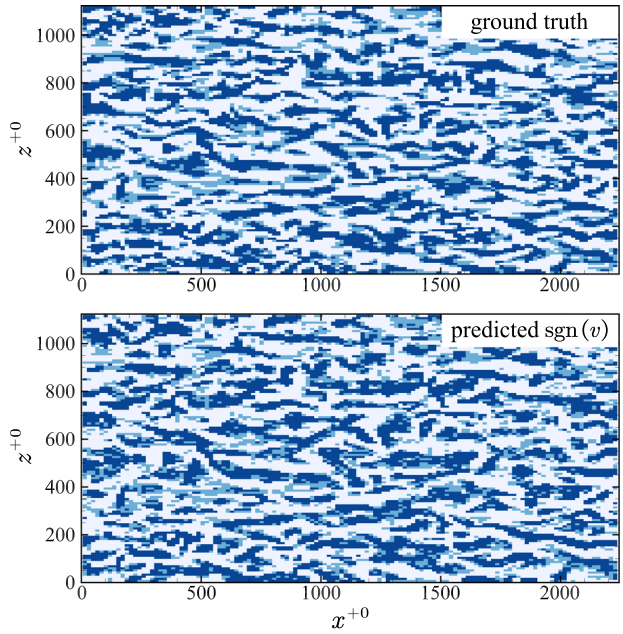

FIG. 12. Comparison between the $sgn(v)$ predicted by the CNN model and the ground truth at a certain instant. The blue regions indicate that the direction of the wall-normal velocity at the detection plane is toward the lower wall, i.e., $sgn(v) = -1$. The dark blue regions indicate that the value of the wall-normal velocity is less than $-0.1u_{\tau 0}$. The instantaneous prediction accuracies with and without considering the wall-normal velocity in $[-0.1u_{\tau 0}, 0.1u_{\tau 0}]$ are 76.9% and 85.1%, respectively.

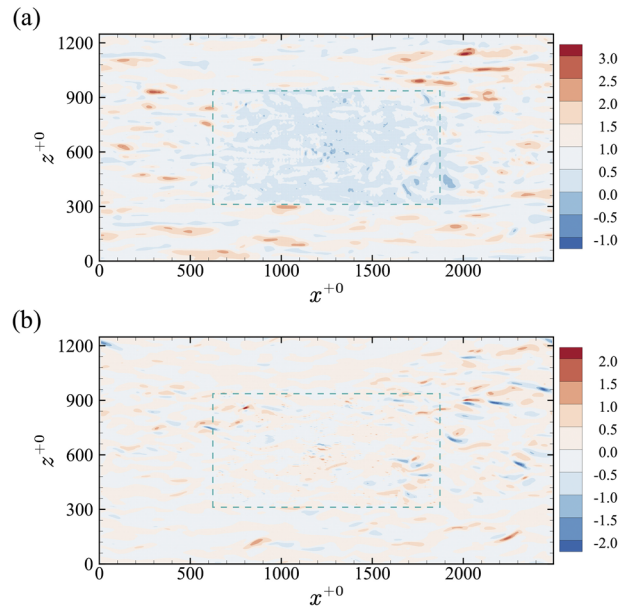

FIG. 13. The distribution of (a) $\partial u^{+0}/\partial y^{+0}$ and (b) $\partial w^{+0}/\partial y^{+0}$ at the lower wall under the opposition blowing scheme with $\alpha = 0$ at a certain instant.

wall-normal, and spanwise directions, respectively. Here, although the domain size is reduced, it is sufficient to capture the change in skin-friction drag, which has been validated by Busse and Sandham.[21] As the grid size in the horizontal direction is larger than the input size of the network, only a quarter of the wall area located at the center of the lower wall is applied with control schemes, i.e., a region with 128 points in both the streamwise and spanwise directions. Figures 13(a) and 13(b) show the instantaneous distribution of $\partial u^{+0}/\partial y^{+0}$ and $\partial w^{+0}/\partial y^{+0}$ under the opposition blowing scheme with $\alpha = 0$, respectively. The dashed rectangle represents the area in which the opposition blowing is applied. In this region, the streamwise wall shear stress is much smaller than that in the surrounding uncontrolled area. In contrast, the difference between the spanwise wall shear stresses in this region and the surrounding uncontrolled area is not obvious.

The time histories of *acc* and the drag reduction results are shown in Figs. 14(a) and 14(b), respectively. *DR* is the average result of the controlled area. When the CNN model trained from the case of $\mathrm{Re}_{\tau 0} = 180$ is implemented to the case of $\mathrm{Re}_{\tau 0} = 396$ without adjusting, the prediction accuracy on the direction of the wall-normal velocity at $y^{+0} = 14.3$ is about 60% (legend "network"). Without considering the wall-normal velocity in $[-0.1u_{\tau 0}, 0.1u_{\tau 0}]$ and

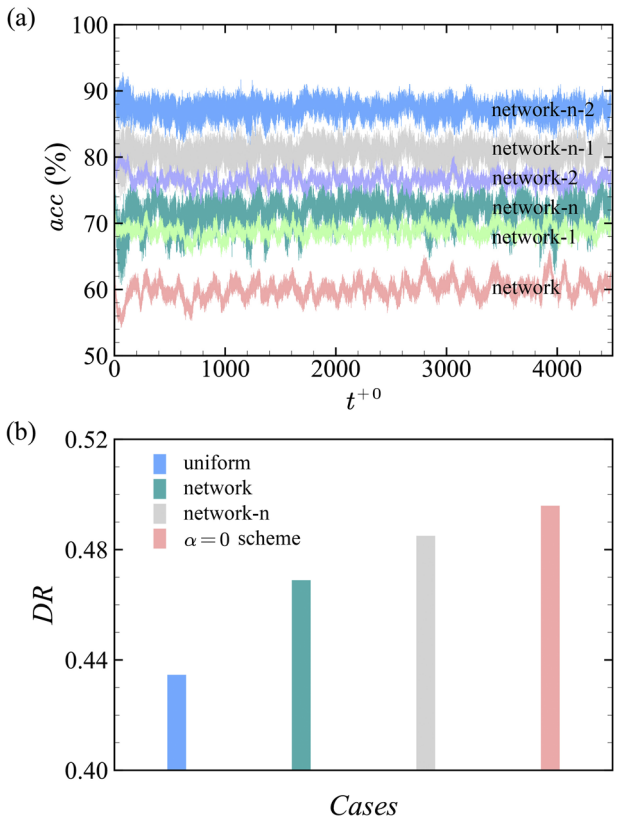

FIG. 14. (a) Time histories of *acc* when the CNN model is implemented to predict the sign of the wall-normal velocity at the plane of $y^{+0} = 14.3$ in the case of $\mathrm{Re}_{\tau 0} = 396$. (b) Comparison of the drag reduction results under different control schemes when $BF = 0.005\rho U_b$.

$[-0.2u_{\tau 0}, 0.2u_{\tau 0}]$, the accuracy can reach 69% (legend "network-1") and 77% (legend "network-2"), respectively. Under $BF = 0.005\rho U_b$, DR obtained by the deep learning based opposition blowing scheme is ~0.47, which improves the drag reduction by about 8% compared to the value of the uniform blowing. This result once again demonstrates that the drag reduction can be improved as long as the location of large wall-normal velocity fluctuations can be accurately predicted. In order to improve the performance of the CNN model, an operation similar to the case of $\mathrm{Re}_{\tau 0} = 180$ is conducted, that is, the actual evolution of the flow field when the opposition blowing scheme is directed by the CNN model is used as the new training set. As a result, the above accuracy is correspondingly increased to 72% (legend "network-n"), 81% (legend "network-n-1"), and 87% (legend "network-n-2"), respectively. The drag reduction is also improved.

V. CONCLUSIONS

Through direct numerical simulation, we performed a detailed investigation of drag reduction by the blowing-only opposition control scheme in turbulent channel flow. Based on the drag reduction characteristics, a simplified opposition blowing scheme is implemented through a convolutional neural network.

First, in order to investigate the influence of the allocation of the blowing velocity on drag reduction under a constant blowing mass flux, the opposition blowing scheme is designed and its drag reduction performances are investigated. The results show that the drag reduction increases monotonically as the distance from the detection plane to the wall decreases and is almost unaffected by the allocation of the blowing velocity. This feature provides great convenience for the implementation of the CNN, which only needs to predict the direction of the wall-normal velocity at the detection plane. As the fluid on the downward moving side of the quasi-streamwise vortices is opposed by the opposition blowing, the skin-friction drag reduces significantly. Nevertheless, the vortices in the near-wall region are strengthened by the continuous injection of the low-speed fluid.

Then, the reasonability of the selected input and output characteristic quantities of the CNN model is verified from a statistical perspective. Based on the statistical properties of turbulent channel flow, the velocity–vorticity–vorticity correlation characterizes the relationship between the distribution of shear stresses in the channel and the wall-normal velocity at the reference plane. A noteworthy feature is that the distribution of the correlation coefficient R_{213} along the spanwise direction presents a stable pattern. This property can be taken as a physical explanation for the neural network to correlate the wall shear stresses with the wall-normal velocity at the detection plane.

Finally, a CNN model is constructed to predict the direction of the wall-normal velocity at the detection plane so as to realize the opposition blowing scheme. It is demonstrated that the CNN model has high accuracy in predicting the direction of the wall-normal velocity at the detection plane on the whole dataset. By adjusting the training set, the drag reduction achieved by the deep learning based opposition blowing scheme is about 19% higher than that of the uniform blowing under the condition of constant blowing mass flux. Additionally, applying the trained network model to a flow at a higher Reynolds number than the training set can still accurately predict the directions of the large wall-normal velocity fluctuations and improve the drag reduction. Thus, the high prediction accuracy of the CNN model for large wall-normal velocity fluctuations can provide effective guidance for the practical application of opposition control.

ACKNOWLEDGMENTS

The authors thank Dr. Y. Yang and Dr. Y. Zhao for valuable discussions. This work was supported by the National Natural Science Foundation of China (NSFC) under Grant Nos. 11988102, 91848201, 11521202, 11872004, and 11802004 and the Beijing Natural Science Foundation under Grant No. L172002. The numerical simulations were performed on the High-Performance Computing Platform of Peking University.

APPENDIX A: DRAG REDUCTION CHARACTERISTICS OF OPPOSITION BLOWING

In order to show that the interaction between the lower and upper parts of the turbulent channel flow caused by the asymmetric boundary conditions does not affect the drag reduction characteristics of opposition blowing, the following cases are conducted. Considering the turbulent channel flow at $\mathrm{Re}_{\tau 0} = 396$, both blowing and suction are applied at local regions of both the upper and lower walls of the channel, and the wall-normal mass flux at each wall is zero. The areas of the blowing region and the suction region are the same, and both are square regions with a side length of $3\pi h/4$. This approach ensures that the boundary conditions of the upper and lower walls are symmetric. In the blowing region, both uniform blowing and opposition blowing are considered, while in the suction region, the boundary condition is always uniform suction, as shown in Fig. 15.

The drag reduction of the uniform blowing and opposition blowing schemes in the blowing region is shown in Fig. 16, in which the opposition blowing scheme considers six situations, i.e., $\alpha = 0$, 0.2, 0.4, 0.6, 0.8, and 1.0. The blowing mass flux in the blowing region remains constant, i.e., $BF = 0.005\rho U_b$. The results show that the drag reduction of opposition blowing is higher than that of uniform blowing, and it is almost independent of the allocation of the blowing velocity among all the effective blowing points. There is an

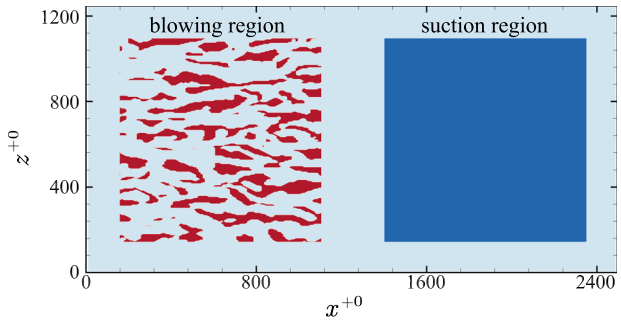

FIG. 15. Instantaneous distribution of the wall-normal velocity at the lower wall of the channel. In the blowing region, the flow is under the control of the opposition blowing scheme with $\alpha = 0$ and $y_d^{+0} = 14.3$. The red color regions represent the instantaneous distribution of the blowing points.

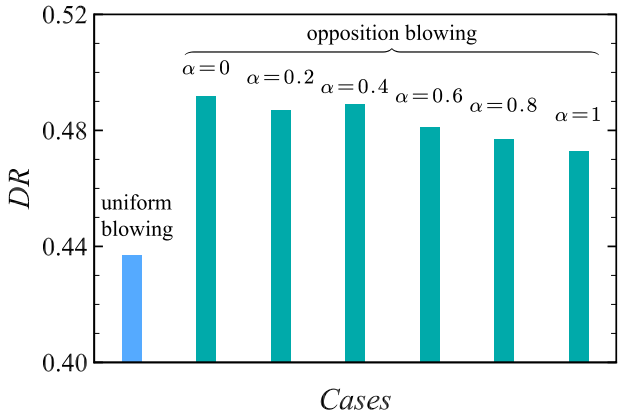

FIG. 16. *DR* of the uniform blowing and opposition blowing schemes in the blowing region of the lower wall.

unobvious trend that the drag reduction decreases slightly as α increases. This characteristic is the same as that obtained from the cases of blowing at the lower wall and suction at the upper wall. Therefore, it is reasonable to believe that the conclusions on drag reduction characteristics in the current work are relatively robust.

APPENDIX B: GIBBS PHENOMENA

In the current work, the boundary conditions are given in the physical space, while the flow field calculation is carried out in the spectral space. Therefore, it is necessary to ensure that the DNS results are not affected by the Gibbs phenomena. The magnitude of the Gibbs phenomena can be measured by evaluating the differences between the original boundary condition given in the physical space and the value after the forward and inverse Fourier transforms. In the circumstance of stochastic blowing with $AF = 0.1$, the blowing velocity at the wall becomes substantially discontinuous. The instantaneous distributions of the wall-normal velocity at the boundary before and after the transforms are shown in Fig. 17. The values of the velocity are highly identical.

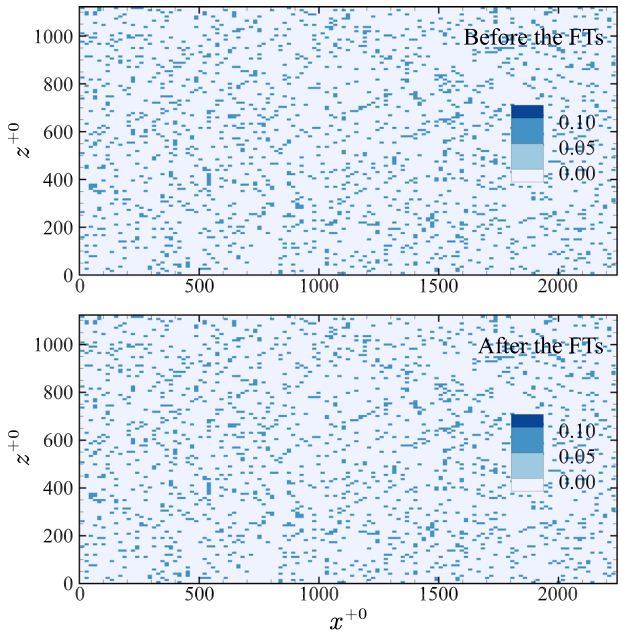

FIG. 17. The wall-normal velocity distributions (normalized by the bulk mean velocity) at the boundary before and after the transforms. "FTs" represents the forward and inverse Fourier transforms.

The root-mean-square-error of the differences of the wall-normal velocity at the boundary before and after the transforms is defined as $RMSE_{FT}$,

$$RMSE_{FT} = \sqrt{\frac{1}{N_x N_z}\sum_{i,k=1,1}^{N_x,N_z}\left[v(i,0,k) - v_{BC}(i,0,k)\right]^2}, \qquad \text{(B1)}$$

where $v_{BC}(i,0,k)$ and $v(i,0,k)$ are the wall-normal velocity distributions at the boundary before and after the transforms, respectively. The calculation results show that the dimensionless value of $RMSE_{FT}$ normalized by the bulk mean velocity is about 1.4×10^{-16}, which is far less than the average blowing velocity. The negligible deviation comes from the fact that after the Fourier transforms, the specified zero velocity at the wall is no longer strictly zero. Hence, in the current work, the Gibbs phenomena have been eliminated.

DATA AVAILABILITY

The data that support the findings of this study are available from the corresponding author upon reasonable request.

REFERENCES

[1] J. Kim, P. Moin, and R. Moser, "Turbulence statistics in fully developed channel flow at low Reynolds number," J. Fluid Mech. **177**, 133 (1987).
[2] S. K. Robinson, "Coherent motions in the turbulent boundary layer," Annu. Rev. Fluid Mech. **23**, 601 (1991).
[3] J. Hong, J. Katz, C. Meneveau, and M. P. Schultz, "Coherent structures and associated subgrid-scale energy transfer in a rough-wall turbulent channel flow," J. Fluid Mech. **712**, 92 (2012).
[4] K.-S. Choi, "Near-wall structure of turbulent boundary layer with spanwise-wall oscillation," Phys. Fluids **14**, 2530 (2002).
[5] J.-I. Choi, C.-X. Xu, and H. J. Sung, "Drag reduction by spanwise wall oscillation in wall-bounded turbulent flows," AIAA J. **40**, 842 (2002).
[6] C. Viotti, M. Quadrio, and P. Luchini, "Streamwise oscillation of spanwise velocity at the wall of a channel for turbulent drag reduction," Phys. Fluids **21**, 115109 (2009).
[7] E. Touber and M. A. Leschziner, "Near-wall streak modification by spanwise oscillatory wall motion and drag-reduction mechanisms," J. Fluid Mech. **693**, 150 (2012).
[8] K. U. Kempaiah, F. Scarano, G. E. Elsinga, B. W. van Oudheusden, and L. Bermel, "3-dimensional particle image velocimetry based evaluation of turbulent skin-friction reduction by spanwise wall oscillation," Phys. Fluids **32**, 085111 (2020).
[9] M.-X. Zhao, W.-X. Huang, and C.-X. Xu, "Drag reduction in turbulent flows along a cylinder by streamwise-travelling waves of circumferential wall velocity," J. Fluid Mech. **862**, 75 (2019).
[10] H. Choi, P. Moin, and J. Kim, "Active turbulence control for drag reduction in wall-bounded flows," J. Fluid Mech. **262**, 75 (1994).
[11] Y. Chang, S. S. Collis, and S. Ramakrishnan, "Viscous effects in control of near-wall turbulence," Phys. Fluids **14**, 4069 (2002).

[12]M. Pamiès, E. Garnier, A. Merlen, and P. Sagaut, "Response of a spatially developing turbulent boundary layer to active control strategies in the framework of opposition control," Phys. Fluids **19**, 108102 (2007).
[13]Y. M. Chung and T. Talha, "Effectiveness of active flow control for turbulent skin friction drag reduction," Phys. Fluids **23**, 025102 (2011).
[14]B.-Q. Deng, C.-X. Xu, W.-X. Huang, and G.-X. Cui, "Strengthened opposition control for skin-friction reduction in wall-bounded turbulent flows," J. Turbul. **15**, 122 (2014).
[15]A. Stroh, B. Frohnapfel, P. Schlatter, and Y. Hasegawa, "A comparison of opposition control in turbulent boundary layer and turbulent channel flow," Phys. Fluids **27**, 075101 (2015).
[16]J. Lee, "Opposition control of turbulent wall-bounded flow using upstream sensor," J. Mech. Sci. Technol. **29**, 4729 (2015).
[17]Y.-S. Wang, W.-X. Huang, and C.-X. Xu, "Active control for drag reduction in turbulent channel flow: The opposition control schemes revisited," Fluid Dyn. Res. **48**, 055501 (2016).
[18]E. Kim and H. Choi, "Linear proportional-integral control for skin-friction reduction in a turbulent channel flow," J. Fluid Mech. **814**, 430 (2017).
[19]H. Li, S. Ji, X. Tan, Z. Li, Y. Xiang, P. Lv, and H. Duan, "Effect of Reynolds number on drag reduction in turbulent boundary layer flow over liquid-gas interface," Phys. Fluids **32**, 122111 (2020).
[20]R. J. Daniello, N. E. Waterhouse, and J. P. Rothstein, "Drag reduction in turbulent flows over superhydrophobic surfaces," Phys. Fluids **21**, 085103 (2009).
[21]A. Busse and N. D. Sandham, "Influence of an anisotropic slip-length boundary condition on turbulent channel flow," Phys. Fluids **24**, 055111 (2012).
[22]H. Park, H. Park, and J. Kim, "A numerical study of the effects of superhydrophobic surface on skin-friction drag in turbulent channel flow," Phys. Fluids **25**, 110815 (2013).
[23]P. Lv, Y. Xue, Y. Shi, H. Lin, and H. Duan, "Metastable states and wetting transition of submerged superhydrophobic structures," Phys. Rev. Lett. **112**, 196101 (2014).
[24]Z. Li, S. Ji, H. Duan, S. Lan, J. Zhang, and P. Lv, "Coupling effect of wall slip and spanwise oscillation on drag reduction in turbulent channel flow," Phys. Rev. Fluids **5**, 124601 (2020).
[25]H. Li, Z. Li, X. Tan, X. Wang, S. Huang, Y. Xiang, P. Lv, and H. Duan, "Three-dimensional backflow at liquid–gas interface induced by surfactant," J. Fluid Mech. **899**, A8 (2020).
[26]P. A. Bullee, R. A. Verschoof, D. Bakhuis, S. G. Huisman, C. Sun, R. G. H. Lammertink, and D. Lohse, "Bubbly drag reduction using a hydrophobic inner cylinder in Taylor-Couette turbulence," J. Fluid Mech. **883**, A61 (2020).
[27]W. A. Rowin and S. Ghaemi, "Effect of Reynolds number on turbulent channel flow over a superhydrophobic surface," Phys. Fluids **32**, 075105 (2020).
[28]Y. Kametani and K. Fukagata, "Direct numerical simulation of spatially developing turbulent boundary layers with uniform blowing or suction," J. Fluid Mech. **681**, 154 (2011).
[29]Y. Sumitani and N. Kasagi, "Direct numerical simulation of turbulent transport with uniform wall injection and suction," AIAA J. **33**, 1220 (1995).
[30]Y. Kametani, K. Fukagata, R. Örlü, and P. Schlatter, "Effect of uniform blowing/suction in a turbulent boundary layer at moderate Reynolds number," Int. J. Heat Fluid Flow **55**, 132 (2015).
[31]A. Stroh, Y. Hasegawa, P. Schlatter, and B. Frohnapfel, "Global effect of local skin friction drag reduction in spatially developing turbulent boundary layer," J. Fluid Mech. **805**, 303 (2016).
[32]Y. Kametani, A. Kotake, K. Fukagata, and N. Tokugawa, "Drag reduction capability of uniform blowing in supersonic wall-bounded turbulent flows," Phys. Rev. Fluids **2**, 123904 (2017).
[33]D. P. Hwang, "Skin-friction reduction by a micro-blowing technique," AIAA J. **36**, 480 (1997).
[34]K. Eto, Y. Kondo, and K. Fukagata, "Assessment of friction drag reduction on a Clark-Y airfoil by uniform blowing," AIAA J. **57**, 2774 (2019).
[35]A. G. Kravchenko, H. Choi, and P. Moin, "On the relation of near-wall streamwise vortices to wall skin friction in turbulent boundary layers," Phys. Fluids A **5**, 3307 (1993).
[36]P. Orlandi and J. Jiménez, "On the generation of turbulent wall friction," Phys. Fluids **6**, 634 (1994).
[37]K. Fukagata, K. Iwamoto, and N. Kasagi, "Contribution of Reynolds stress distribution to the skin friction in wall-bounded flows," Phys. Fluids **14**, L73 (2002).
[38]J. Kim, "Physics and control of wall turbulence for drag reduction," Philos. Trans. R. Soc., A **369**, 1396 (2011).
[39]C. Lee, J. Kim, D. Babcock, and R. Goodman, "Application of neural networks to turbulence control for drag reduction," Phys. Fluids **9**, 1740 (1997).
[40]C. Lee, J. Kim, and H. Choi, "Suboptimal control of turbulent channel flow for drag reduction," J. Fluid Mech. **358**, 245 (1998).
[41]K. H. Lee, L. Cortelezzi, J. Kim, and J. Speyer, "Application of reduced-order controller to turbulent flows for drag reduction," Phys. Fluids **13**, 1321 (2001).
[42]K. Fukagata and N. Kasagi, "Suboptimal control for drag reduction via suppression of near-wall Reynolds shear stress," Int. J. Heat Fluid Flow **25**, 341 (2004).
[43]L. V. Lorang, B. Podvin, and P. Le Quéré, "Application of compact neural network for drag reduction in a turbulent channel flow at low Reynolds numbers," Phys. Fluids **20**, 045104 (2008).
[44]N. Kasagi, Y. Suzuki, and K. Fukagata, "Microelectromechanical systems-based feedback control of turbulence for skin friction reduction," Annu. Rev. Fluid Mech. **41**, 231 (2009).
[45]M. Frank, D. Drikakis, and V. Charissis, "Machine-learning methods for computational science and engineering," Computation **8**, 15 (2020).
[46]P. A. Srinivasan, L. Guastoni, H. Azizpour, P. Schlatter, and R. Vinuesa, "Predictions of turbulent shear flows using deep neural networks," Phys. Rev. Fluids **4**, 054603 (2019).
[47]J. Huang, H. Liu, and W. Cai, "Online *in situ* prediction of 3-D flame evolution from its history 2-D projections via deep learning," J. Fluid Mech. **875**, R2 (2019).
[48]J.-Z. Peng, S. Chen, N. Aubry, Z.-H. Chen, and W.-T. Wu, "Time-variant prediction of flow over an airfoil using deep neural network," Phys. Fluids **32**, 123602 (2020).
[49]V. Sekar, Q. Jiang, C. Shu, and B. C. Khoo, "Fast flow field prediction over airfoils using deep learning approach," Phys. Fluids **31**, 057103 (2019).
[50]B. Liu, J. Tang, H. Huang, and X.-Y. Lu, "Deep learning methods for super-resolution reconstruction of turbulent flows," Phys. Fluids **32**, 025105 (2020).
[51]S. R. Bukka, R. Gupta, A. R. Magee, and R. K. Jaiman, "Assessment of unsteady flow predictions using hybrid deep learning based reduced-order models," Phys. Fluids **33**, 013601 (2021).
[52]M. P. Brenner, J. D. Eldredge, and J. B. Freund, "Perspective on machine learning for advancing fluid mechanics," Phys. Rev. Fluids **4**, 100501 (2019).
[53]S. L. Brunton, B. R. Noack, and P. Koumoutsakos, "Machine learning for fluid mechanics," Annu. Rev. Fluid Mech. **52**, 477 (2020).
[54]K. Fukami, T. Nakamura, and K. Fukagata, "Convolutional neural network based hierarchical autoencoder for nonlinear mode decomposition of fluid field data," Phys. Fluids **32**, 095110 (2020).
[55]H. Eivazi, H. Veisi, M. H. Naderi, and V. Esfahanian, "Deep neural networks for nonlinear model order reduction of unsteady flows," Phys. Fluids **32**, 105104 (2020).
[56]M. Yu, W.-X. Huang, and C.-X. Xu, "Data-driven construction of a reduced-order model for supersonic boundary layer transition," J. Fluid Mech. **874**, 1096 (2019).
[57]A. Güemes, S. Discetti, and A. Ianiro, "Sensing the turbulent large-scale motions with their wall signature," Phys. Fluids **31**, 125112 (2019).
[58]H. Wang, Z. Yang, B. Li, and S. Wang, "Predicting the near-wall velocity of wall turbulence using a neural network for particle image velocimetry," Phys. Fluids **32**, 115105 (2020).
[59]B.-Z. Han and W.-X. Huang, "Active control for drag reduction of turbulent channel flow based on convolutional neural networks," Phys. Fluids **32**, 095108 (2020).
[60]Z. Li, B. Hu, S. Lan, J. Zhang, and J. Huang, "Control of turbulent channel flow using a plasma-based body force," Comput. Fluids **119**, 26 (2015).
[61]J. Jeong and F. Hussain, "On the identification of a vortex," J. Fluid Mech. **285**, 69 (1995).
[62]J. Chen, F. Hussain, J. Pei, and Z.-S. She, "Velocity-vorticity correlation structure in turbulent channel flow," J. Fluid Mech. **742**, 291 (2014).